Generation of Realistic Particle Structures and Simulations of Internal Stress: A Numerical/AFM Study of LiMn₂O₄ Particles

Jeong Hun Seo,[a] Myoungdo Chung,[b] Myounggu Park,[a] Sang Woo Han,[a] Xiangchun Zhang,[*,b] and Ann Marie Sastry[a,c,d,z]

[a]*Department of Mechanical Engineering,* [c]*Department of Biomedical Engineering, and* [d]*Department of Materials Science and Engineering, University of Michigan, Ann Arbor, Michigan 48109-2125, USA*
[b]*Sakti3, Inc., Ann Arbor, Michigan 48108, USA*

In this paper, the real geometries of cathode particles are reconstructed using atomic force microscopy (AFM). Finite element analysis of intercalation-induced stress is applied to the reconstructed realistic geometries of single and aggregated particles. The reconstructed particle geometry shows rugged surfaces at the boundary for Li-ion flux, which cause larger surface areas than smooth particles. The finite element model of a LiMn₂O₄ system is simulated under galvanostatic and potentiodynamic control. To investigate the realistic level of boundary flux at particle scale, the macroscale simulation results are also applied to intercalation-induced stress analysis of real cathode particles. The numerical results of intercalation-induced stress show that the von Mises stress is concentrated at sharply dented boundaries due to curvature effects when Li ions intercalate or deintercalate and is an order-of-magnitude higher in realistic particle geometries than the stress in ideal smooth particles. It has also been shown that the stress under potentiodynamic control is higher than the stress under galvanostatic control because the high Li-ion flux at two plateaus in the open-circuit potential of a LiMn₂O₄ system results from linear voltage sweep. We also present results showing that some mesh architectures are preferred for handling these potentially singular regions.
© 2011 The Electrochemical Society. [DOI: 10.1149/1.3552930] All rights reserved.

Particle fractures in active materials have been considered one of the capacity degradation mechanisms in Li-ion batteries,[1] because the disjunction of materials results in loss of electrical contact and breakdown of the surface solid electrolyte interphase (SEI) layers. Cracks in particle structures can be caused in the manufacturing process[2] or by intercalation-induced stress.[3–7] The intercalation-induced stress during Li-ion battery cycles can cause crack propagation and particle fracture, since the microstructural strain accumulates over cycles[8,9] and the induced-stress could surpass the yield strength of active materials.[3] However, their origin and their effect on capacity degradation are not fully understood.

Experiments have revealed particle fractures in active materials via various analytical techniques. In cathodes, microscale strains[8,10,11] and fissured particles[10,12,13] were observed through transmission electron microscopy and scanning electron microscopy (SEM) studies. Also in anodes, structural disordering and cracks in cycled graphite electrodes have been observed through microprobe study,[14] SEM,[15] and acoustic emission technique.[16] Cross-sectional SEM has shown that fractures took place near the separator and penetrated into electrodes.[14] Despite these observations of mechanical failures in electrode particles, particle fracture has not been clearly correlated to capacity degradation of Li-ion batteries.

The intercalation and deintercalation of Li ions have been analyzed using a thermal analogy,[5–7] investigating smooth particles such as spheres[7] or ellipsoids.[5,6] Furthermore, the mechanical stress in ideal spherical particles is modeled and coupled with the electrochemical kinetics at cell scale.[14,15] The microscale strain within spherical particles is coupled with macroscale effective strain for simulating cell performance under external mechanical boundary conditions.[16] However, smooth particle geometry does not yield the concentrated stress at surfaces that are suspected as a cause of capacity degradation. Unlike the smooth geometry considered in the literature, real particles have multiple convex and concave surfaces, which cause larger surface area for Li-ion flux at particle boundaries. At microscale (i.e., scales of aggregated particles), three-dimensional microstructures of real composite electrodes have been reconstructed using focused-ion beam/scanning electron microscopy (FIB/SEM)[17–19] and x-ray tomography.[20] FIB/SEM of LiCoO₂ has shown microstructural degradation.[17] The reconstructed micro-

structures are used to extract the microstructure information (e.g., such as porosity, interfacial area, and tortuosity) that is used to calculate effective material properties such as effective ionic diffusivity and conductivity. At particle scale, in situ atomic force microscopy (AFM) study has shown dimensional changes in LiCoO₂ particles during Li-ion deintercalation.[21] Diffusion coefficient and its geometry are measured through AFM study of a single particle LiMn₂O₄ electrode.[22]

However, these microscale reconstruction studies did not investigate or simulate intercalation-induced stress within microstructures at realistic levels and were analyzed as a correlate of particle fracture at particle scale. Thus, the goal of this work is to investigate the intercalation-induced stress within realistic particle structures. Our specific objectives are threefold:

(1) Reconstruct real geometries of cathode materials using AFM;
(2) Apply finite element analysis of intercalation-induced stress to the realistic geometry of single particles and an aggregated particle; and
(3) Map the response of complex particle geometry to realistic loads/strains.

To investigate the effect of finite elements on the surface representation in complex particle geometry, we conducted two case studies in discretization of the analysis domain: hexahedral and tetrahedral. Hexahedral finite elements have been commonly used for mesh uniformity in the complex geometries typical in classical composite materials[23] and biologic materials (e.g., bone tissues[24]). The hexahedral approach (i.e., voxel approach) has been used to build a regular finite element mesh of spatially irregular geometry.[25]

Method

AFM sample preparation.— LiMn₂O₄ particle samples were prepared by embedding isolated particles on a gold foil via the following steps. First, LiMn₂O₄ powder (99.5%, Alfa Aesar) was dispersed in acetone suspension with a ratio of 1% wt by using an ultrasonic wave for 60 min, then the LiMn₂O₄ particles were placed onto a gold foil (99.99%, Aldrich) from a drop of suspension and covered with another gold foil. By applying gradual compression using a preprogrammed compressor (Instron) the electrode particles were embedded on the gold foil. Once the top gold foil was

* Electrochemical Society Active Member.
z E-mail: amsastry@umich.edu

carefully removed, the particle-topped substrate was examined by SEM for larger scale observation before being scanned using AFM.

AFM imaging.— AFM (MultiMode coupled with a NanoScope controller, Veeco) on particle-topped substrate was used to reconstruct the 3D particle geometry. Sample particles in the dispersed $LiMn_2O_4$ were first located using optical microscopy, and then tapping mode AFM was applied over a larger area (up to 30 μm by 30 μm) to find the exact location of the particle. Higher resolution 3D particle images were obtained by optimizing the scanning condition (i.e., adjusting scan rate and probe set point). The scanned AFM image provides z coordinates of uniformly distributed sampling points that were used to reconstruct particle geometries.

Reconstruction of particle geometry and generation of finite element mesh.—AFM imaging provides clouds of surface points that are uniformly distributed. With these points, two types of finite element mesh can be constructed: tetrahedral and hexahedral (voxel). Tetrahedral mesh requires particle surface reconstruction using the clouds of surface points. In order to accurately capture the detailed surface, a large number of triangular surfaces were automatically generated by scripting commands in HYPERMESH software. Then, the constructed surfaces were adequately discretized using HYPERMESH for generating a tetrahedral finite element mesh within the particle geometry. Voxel element mesh does not need to build the particle surfaces before generating finite element mesh. Unlike tetrahedral meshing, voxel meshing directly uses clouds of surface points for discretizing the analysis domain. According to the resolution of these surface points in the x–y plane, the size of uniform voxel elements can be determined. The heights (z coordinates) of surface points are equally discretized by the determined size of these voxel elements. This creates a regular finite element mesh. Figure 1 shows examples of two different finite element meshes for reconstructing a sphere.

Finite element analysis of intercalation-induced stress.— In previous studies,[5,6] we applied galvanostatic and potentiodynamic control to smooth particles; in this study, we applied the same analysis to the finite element model of a realistic $LiMn_2O_4$ system. Additionally, the local Li-ion fluxes were calculated at three different locations (e.g., near the separator, at the middle of the electrode, and near the current collector) in the macroscale electrode by using pseudo-2D model.[26] Then they were also applied to the reconstructed finite element model of realistic particles, in order to see the stress generation at realistic particle under macroscale discharging simulation.

Li-ion intercalation has been ideally modeled as a diffusion process with boundary flux. In this model, cathode particles are homogeneous, isotropic single-phase particles. Diffusive flux of Li ion is driven by concentration gradients and stress gradients. This flux combined with mass conservation give the following governing equations for diffusion processes

$$\frac{\partial c}{\partial t} + \nabla \cdot \mathbf{J} = 0 \qquad [1]$$

$$\mathbf{J} = -D\left(\nabla c - \frac{\Omega c}{RT}\nabla \sigma_h\right) \qquad [2]$$

where c is the concentration of Li ion, $\mathbf{J}$ is species flux, R is the gas constant, T is temperature, Ω is the partial molar volume of lithium,[6] and σ_h is the hydrostatic stress defined as $\sigma_h = (\sigma_{11}+\sigma_{22}+\sigma_{33})/3$ (where σ_{ij} is the element in stress tensor).

By using the thermal analogy model, the constitutive equation of an elastic model for intercalation analysis can be written

$$\varepsilon_{ij} = \frac{1}{E}\left[(1+\nu)\sigma_{ij} - \nu\sigma_{kk}\delta_{ij}\right] + \frac{\tilde{c}\Omega}{3}\delta_{ij} \qquad [3]$$

where ε_{ij} are strain components, σ_{ij} are stress components, E is Young's modulus, ν is Poisson's ratio, and $\tilde{c} = c - c_0$ is the concentration difference of Li ion from the stress-free value. A Young's modulus $E = 10$ GPa and a partial molar volume $\Omega = 3.497 \times 10^{-6}$ m^3/mol are assumed here.

The above-mentioned equations were modeled and solved using COMSOL MULTIPHYSICS.[27] In this work, linear finite elements for concentration variables and quadratic finite elements for displacement variables were used. Due to the limitation of an AFM scan, only one side of the particle can be reconstructed. Thus, the bottom surface was assumed to be a symmetric plane (i.e., no flux as Li ion penetrates the bottom surface, and the displacement in the plane-normal direction is constrained), while other surfaces had Li-ion flux and were stress-free. Initial concentrations (c_0) are zero under galvanostatic discharge and $0.996c_{max}$ under potentiodynamic charge. Particles are initially stress-free.

Under galvanostatic diffusion of Li ion, the boundary flux at particle surfaces is determined by discharge rate and theoretical capacity of a $LiMn_2O_4$ particle. In order to investigate the surface area effect of a particle system, we construct an oblate ellipsoid and a sphere which had the same volume (i.e., identical theoretical capacity). In the case of the oblate ellipsoid, the depth dimension was fixed and the other dimensions (e.g., width and height) were adjusted to match the volume of the oblate ellipsoid to the corresponding realistic particle. Depth dimension was determined by the longest length of the particle through the in-plane direction. Width dimension was determined in the direction perpendicular to the depth direction. During the discharge cycle (i.e., Li-ion intercalation), the intercalation-induced stress was analyzed by varying the discharge rate from 1 C to 10 C. The boundary flux under galvanostatic control was estimated by the
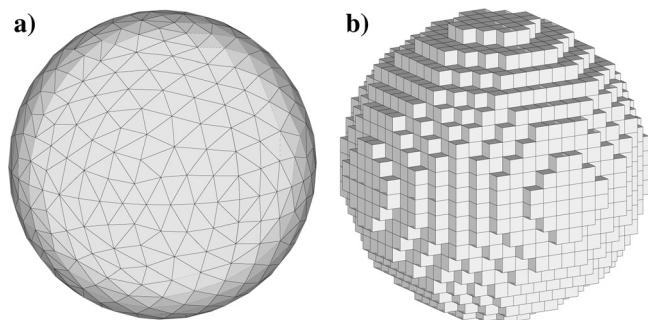

Figure 1. Finite element discretization of sphere with (a) tetrahedral elements and (b) hexahedral elements.
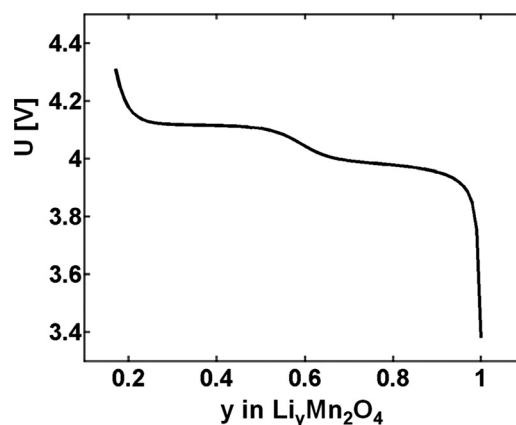

Figure 2. (a) Open-circuit potential of $LiMn_2O_4$ and (b) applied potential with a fixed sweep rate of 0.4 mV between 3.51 and 4.31 V.

Table I. Parameters and material properties for intercalation analysis.

Symbol	Value
D	7.08×10^{-15} m^2/s[a]
c_{max}	2.37×10^{4} mol/m^3[b]
c_{Li}	1000 mol/m^3[b]
c_0	$0.996\, c_{max}$[b]
K	1.9×10^{-9} m$^{5/2}$ s^{-1} mol$^{-1/2}$[b]
β	0.5[b]

[a]Ref. 5.
[b]Ref. 6

$$- n \cdot \mathbf{J}|_{\Gamma} = \frac{C_{rate}C_{th}[Ah]}{A[m^2]F[Ah/mol]3600[s]} \qquad [4]$$

where n is the normal vector at the surface boundary Γ, C_{rate} is the discharge rate, C_{th} is the theoretical capacity of the particle, A is the area of the surface boundary Γ, and F is the Faraday constant.

The potentiodynamic cycle determines the boundary flux by using Butler–Volmer kinetics that governs electrochemical electrolyte reactions at particle surfaces. Electrochemical reaction occurs at the particle surfaces; it is described by the Butler–Volmer equation as

$$\mathbf{J} = \frac{\mathbf{i}_n}{F} = i_0 \left[\exp\left(\frac{(1-\beta)}{RT} \eta \right) - \exp\left(-\frac{\beta}{RT} \eta \right) \right] \qquad [5]$$

where i_0 is exchange current density, η is surface overpotential (i.e., the difference between the applied potential and the equilibrium potential), and β is a symmetry factor representing the fraction of the applied potential that promotes cathodic reaction. Following the microvoltammetric study of a smooth particle,[6] the applied potential
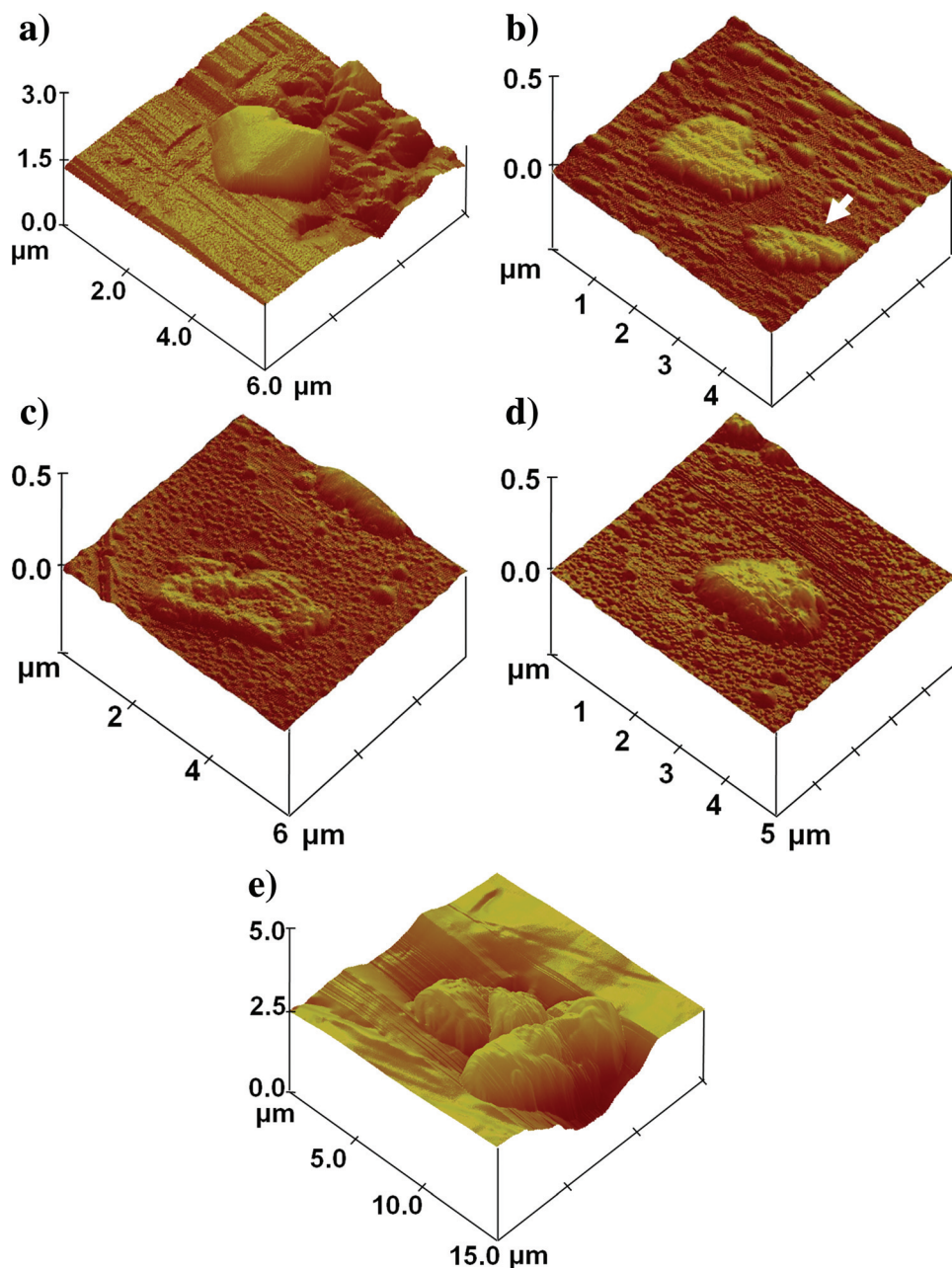

Figure 3. (Color online) AFM-scanned images: (a) single particle (SP-I), (b) single particle (SP-II), (c) single particle (SP-III), (d) single particle (SP-IV), and (e) aggregated particles (MP-I).

Table II. Geometry properties of scanned particles.

Particle	Width [μm]	Depth [μm]	Height [μm]	Volume [μm³]	Surface area [μm²]	Specific interfacial area [μm⁻¹]
SP-I	2.344	2.719	0.543	1.476	6.29	4.26
SP-II	0.941	1.901	0.481	0.309	2.30	7.44
SP-III	1.935	3.171	0.489	1.194	6.43	5.39
SP-IV	1.797	2.188	0.481	0.814	4.30	5.28
MP-I	9.512	10.44	1.346	48.55	82.7	1.70

linearly changes over time under potentiodynamic control; it is assumed that the potential of the solid phase is uniform within particles and the concentration of electrolyte remains constant during the potentiodynamic cycling. We defined the C-rate under potentiodynamic control by using the voltage sweeping time.[6] For example, if the voltage is swept for 1 h, then it is 1 C. The open-circuit potential of $LiMn_2O_4$ is illustrated in Fig. 2.
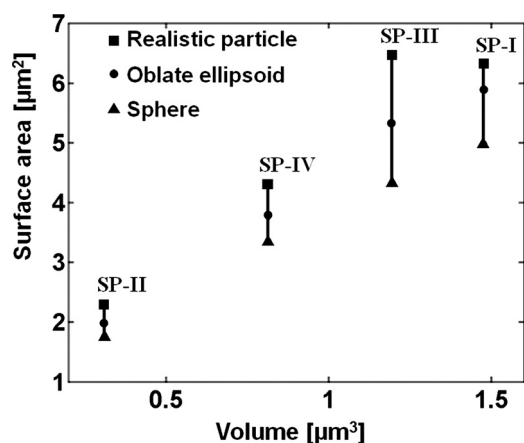
In Eq. 5, the exchange current density i_0 is given by

$$i_0 = Fk(c_1)^{1-\beta}(c_{max,s} - c_{se})^{1-\beta}(c_{se})^{\beta} \qquad [6]$$

where c_1 is the concentration of lithium ion in the electrolyte, c_{se} is the concentration of Li ion on the surface of the solid electrode, c_{max} is the stoichiometric maximum concentration, and k is the reaction rate constant. The values of parameters and material properties are listed in Table I.

Results

AFM scanning of isolated particles.— Four single particles and a three-particle aggregation were scanned using AFM, as shown in Fig. 3. For single particles (Figs. 3a–3d), 5 or 6 μm² areas were scanned while a 15 μm² area was scanned for the particle aggregate (Fig. 3e). Note that the small particle indicated by a white arrow was selected for intercalation-induced stress analysis in Fig. 3b. Individual particle sizes range from 2 to 4 μm. Scanned particles have multiple convex and concave surfaces. V-shaped indents exist on the sides of the particles (e.g., SP-I, SP-II, and MP-I) or the upper surfaces (e.g., SP-III, MP-I). Here, we denote the single particles as SP and the multiple particle structure as MP. SP-I particle has rather smooth surfaces, while the other SP and MP particles have rugged surfaces. The line noises observed along the scanning direction in Figs. 3a, 3d, and 3e are removed by downsampling the clouds of surface points. Since substrates are not smooth at the micron scale, there exist many small bumps in scanned images that require manual identification of the boundaries between scanned particles and substrates.

Geometric properties of scanned particles are listed in Table II. As described in Table II, most of scanned particles are oblate shapes in which the length of the polar axis is shorter than the axes of width and depth. Figure 4 shows the surface area of scanned particles versus their volume. Since the volume is identical, we can see how much the surface increases in realistic $LiMn_2O_4$ particles when the theoretical capacities of particles are fixed. Due to their rugged surface, the surface area of realistic particles is larger than that of oblate ellipsoids and spheres. The surface area of realistic particles is 7–20% larger than the surface area of oblate ellipsoids and 26–48% larger than the surface area of spheres.

Mesh construction of realistic particles.— The discretized finite element mesh of SP-I particle is shown in Fig. 5. The particle geometry of SP-I is used to compare the analysis results with different finite element types (i.e., voxel and tetrahedral). The voxel resolution differs depending on the downsampling size; a downsampling size of 4 was used, as shown in Fig. 5. As expected, the voxel mesh is a jagged approximation of the particle geometry, while the tetrahedral mesh clearly represents the surfaces on the scanned particle geometry. It is noted that no adaptive meshing method is used in this work.

The results of mesh generation for the SP-I particle are summarized in Table III. Compared to the same-volume oblate ellipsoid, the surface area of SP-I particle increased by 7.16% in the tetrahedral mesh. The voxel mesh shows 40.46% larger surface than the tetrahedral mesh, and the degrees of freedom in voxel mesh of the SP-I particle shows an order-of-magnitude difference from the degrees of freedom in tetrahedral mesh of the SP-I particle. This difference results in higher numerical cost and larger memories required in finite element analysis. Because of the symmetries in geometry and boundary conditions, only the quarter domain is modeled in cases of oblate ellipsoids and spheres.

As shown in Fig. 5 and Table III, tetrahedral mesh better represents the particle geometry and uses a smaller number of nodes than voxel mesh. The other single particles, SP-II to SP-IV, and the
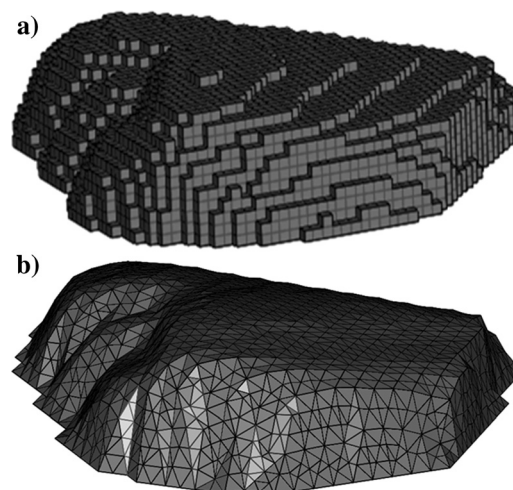

Figure 4. Surface area of scanned particles, oblate ellipsoids, and spheres.

Figure 5. Finite element mesh of SP-I: (a) voxel mesh and (b) tetrahedral mesh.

Table III. Mesh properties of finite element meshes as shown in Fig. 5.

Mesh	Number of elements	Number of degrees of freedom (DOFs)	Avg. volume of finite elements [μm^3]	Surface area [μm^2]
Voxel mesh of SP-I particle	14,337	398,641	1.03×10^{-4}	8.84
Tetrahedral mesh of SP-I particle	14,808	78,575	9.97×10^{-5}	6.29
Tetrahedral mesh of oblate ellipsoid	3,966	20,457	9.30×10^{-5}	5.87
Tetrahedral mesh of sphere	3,955	19,437	9.33×10^{-5}	4.98

particle aggregate MP-I were meshed using tetrahedral elements as illustrated in Figs. 6a–6d. The mesh properties of other single particles and the particle aggregate are summarized in Table IV.

Finite element analysis of intercalation-induced stress.— Under galvanostatic control of Li-ion diffusion, intercalation-induced stress quickly increases and slowly decreases after the surface boundary reaches maximum Li-ion concentration, as shown in Fig. 7. The *x*-axis label "DOD" (i.e., depth of discharge) is calculated by dividing the amount of intercalated Li ions with the corresponding particle capacities. The von Mises stress results were first compared for two different mesh types: voxel versu tetrahedral. During galvanostatic discharge, voxel mesh results show higher stress than those in tetrahedral mesh, but the stress in voxel mesh reaches its maximum more slowly. The maximum von Mises stress occurs at the particle surface as shown in Fig. 8, which is consistent with the results in a previous work.[6] In order to see the stress concentration in the V-shape boundary (i.e., red region in Fig. 8), the smooth point in the SP-I particle was selected and the stresses were compared at two different points: the smooth surface point (i.e., *B* in Fig. 8) and the stress-concentrated region point (i.e., *A* in Fig. 8). As shown in Fig. 9, the maximum von Mises stress at a smooth point is an order-of-magnitude lower than the stress at a point in a sharply dented surface, and thus the stress increment at a smooth point is an order-of-magnitude lower than that in a sharply dented point. Under galvanostatic Li-ion flux, the boundary flux is the same for all surface points. The greater stress at a sharply indented surface is the result of higher curvature because the dented geometry experiences expansion or shrinkage when Li ions intercalate or deintercalate (i.e., curvature effect). As also shown in the distribution of von Mises stress (Fig. 8), the stress increase in voxel mesh is 72.49% higher than the stress increase in tetrahedral mesh. The other difference between voxel and tetrahedral mesh is the jagged distribution

of the von Mises stress on the surface of voxel mesh, while the von Mises stress, as shown in Fig. 8(b), is smoothly distributed on the surface in tetrahedral mesh.

By varying the galvanostatic discharge rate, the von Mises stress at point *B* in SP-I particle was compared with the stress in the corresponding oblate ellipsoid and spherical particles having the same volume as SP-I particle in Fig. 10. The maximum von Mises stress increases monotonically with discharge rate. The maximum von Mises stress in an oblate ellipsoid is 11% higher than the stress in a spherical particle, while the von Mises stress in a realistic particle is 340–380% higher than the stress in a spherical particle. Maximum von Mises stress versus surface area in single particles under 5 C galvanostatic discharge is compared in Fig. 11. As also revealed in Fig. 10, maximum von Mises stress increases as surface area increases. The SP-III particle has the biggest increase of surface area compared to the corresponding sphere, and this severe ruggedness results in the midvalued stress (i.e., green color) on its surface. In contrast, the SP-I particle shows more distribution of low stress (i.e., blue color) on its surface. The SP-I particle shows the biggest stress increase from smooth particles among scanned particles, because it has the sharpest valley on the particle surface. In the case of the SP-II particle, the smooth ellipsoid is a prolate shape while the other single particles are an oblate shape. Due to this shape, the stress in the ellipsoid is less than the stress in the sphere because the stress decreases as the aspect ratio increases in a prolate ellipsoid.[6]

During potentiodynamic control of Li-ion diffusion, the stress within particles experiences two peaks due to the two plateaus in open-circuit potential of LiMn$_2$O$_4$ and reaches its maximum at the second peak as shown in Fig. 12. The Li-ion flux under potentiodynamic control is determined by the Butler–Volmer equation, which is exponential with surface overpotential. The applied potential linearly increases and causes high surface overpotential at two plateaus in the open-circuit potential. Thus, high Li-ion flux resulting
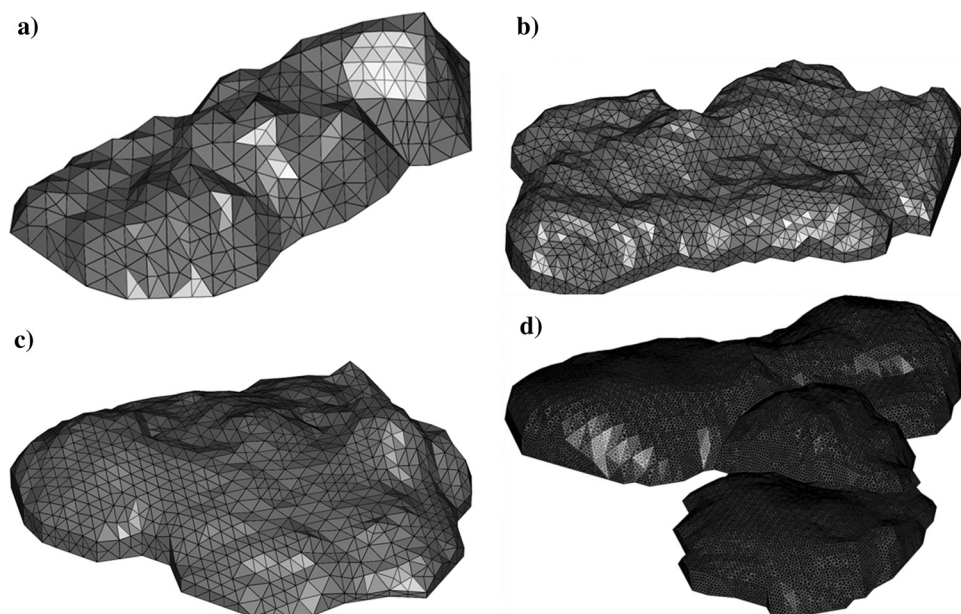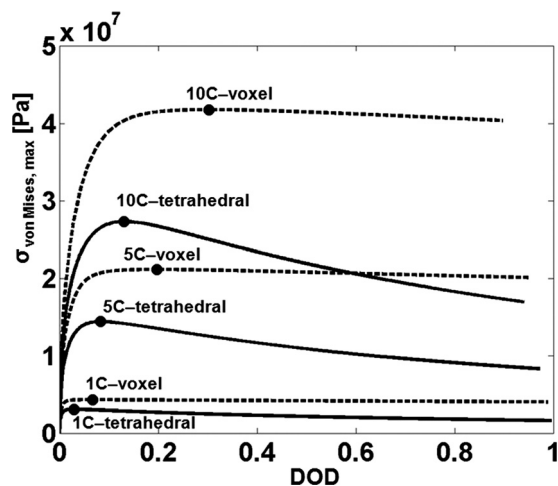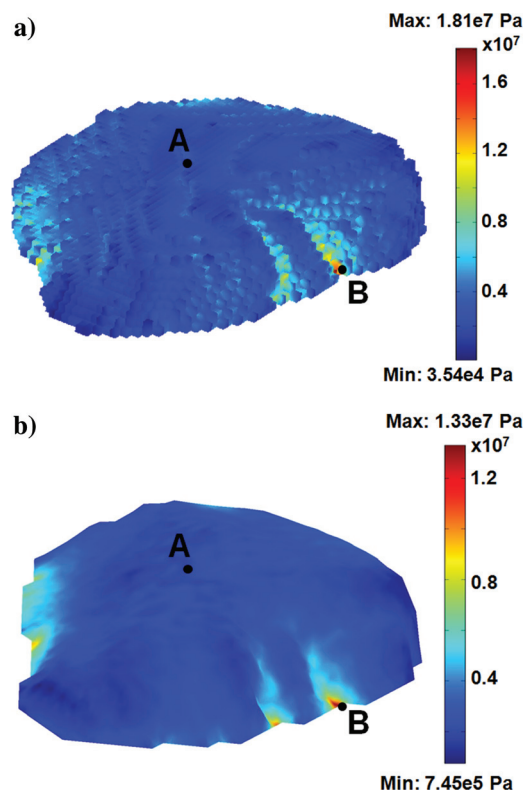

Figure 6. Tetrahedral finite element mesh: (a) SP-II, (b) SP-III, (c) SP-IV, and (d) MP-I.

Table IV. Total number of elements and nodes in the finite element meshes as shown in Fig. 6.

Particles	Number of finite elements	Number of DOFs
SP-II	20,544	18,056
SP-III	38,402	64,901
SP-IV	25,063	44,407
MP-I	45,060	234,277

from linear voltage sweep leads to two stress peaks at two plateaus.[6] Under the same C rate, the stress generated by potentiodynamic control is higher than that generated by galvanostatic control, because the linearly-varying potentiodynamic control results in larger Li-ion flux at the plateaus of open-circuit potential than the flux under galvanostatic control. In the manner shown in Fig. 10. Figure 13 shows maximum von Mises stresses in the SP-I particle, oblate ellipsoid, and sphere. The maximum von Mises stress in an oblate ellipsoid is 3–5% higher than the stress in a spherical particle at high C rate (i.e., 5 C and 10 C), while the von Mises stress in a realistic particle is 73–82% higher than the stress in a spherical particle. Maximum von Mises stress versus surface area in single particles under 5 C potentiodynamic charge is compared in Fig. 14. Like the galvanostatic diffusion, maximum von Mises stress increases as surface area increases. When the applied potential sweeps the plateau regions under potentiodynamic control, the boundary flux highly increases due to the increase in surface overpotential, while the boundary flux is constant under galvanostatic control. Accordingly, the higher boundary flux under potentiodynamic control causes higher stress than constant-flux galvanostatic control. Thus, the stress under potentiodynamic control is higher than the stress under galvanostatic control. Figure 15 shows the stress distributions on particle surfaces at the second peak of the von Mises stress. As already shown in Fig. 7, maximum von Mises stress occurs at the sharply indented points in single particles SP-II to SP-IV and the particle-aggregate MP-I.

5 C-rate constant current discharge is simulated using the pseudo-2D model.[26] As a result of this macroscale simulation, Li-ion fluxes are different from the locations at electrodes as shown in Fig. 16a. Note that Li-ion flux is expressed as a concentration flux unit by dividing current flux with Faraday constant F. The local Li-ion flux near the separator (i.e., point a) is significantly higher than other points (i.e., points b and c). As a result, the maximum von Mises stress within the particle under these fluxes quickly reaches 142 MPa as shown in Fig. 16b, which is a lot higher than the stress

Figure 8. (Color online) von Mises stress distribution of single particle SP-I discretized by (a) voxel mesh (DOD = 0.2) and (b) tetrahedral mesh (DOD = 0.08) under 5 C galvanostatic discharge.

under single particle galvanostatic discharge or potentiodynamic charge as shown in Figs. 10 and 13.

Discussion

In the sample preparation, gradual compression could have made realistic particle shapes oblate when they were placed into the gold substrate. Thus, this compression process is likely to be the reason that all scanned particles in this work are flat and low. Since AFM scanning reveals only the upper part of realistic particles, we used the assumption that the bottom surface is the

Figure 7. Maximum von Mises stress during galvanostatic discharge in particle SP-I for three discharge rates: 1 C, 5 C and 10 C
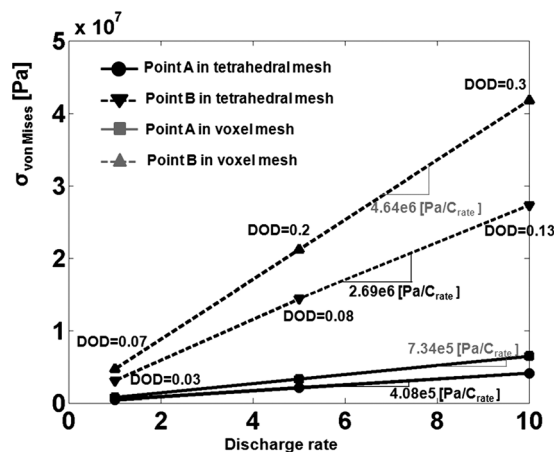
Figure 9. von Mises stress at points A and B in particle SP-I for three galvanostatic discharge rates: 1 C, 5 C, and 10 C.

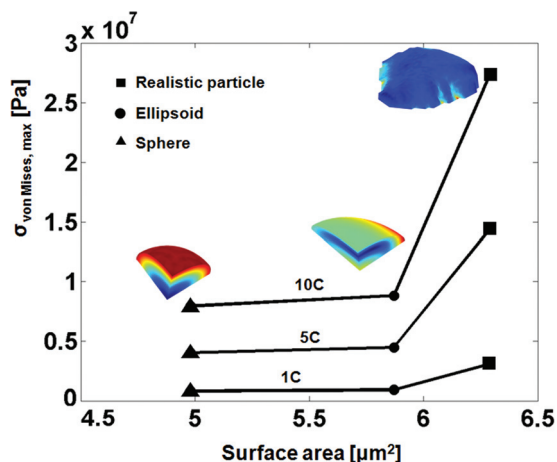**Figure 10.** (Color online) Maximum von Mises stress in particle SP-I, oblate ellipsoid, and sphere by varying galvanostatic discharge rate.

Figure 12. Maximum von Mises stress during potentiodynamic charge in SP-I particle for three charge rates: 1 C, 5 C, and 10 C

symmetric plane of the realistic particles in this finite element simulation requiring *z*-direction displacement constraints and zero flux through the symmetric plane. Thus, the particle surface reconstruction was not complete with AFM scanning. However, the particle was pressed and the underside of the scanned particle was immersed in the gold substrate. Thus the underside of the particle could not take Li-ion flux at the boundary. So, the zero-flux assumption and *z*-directional displacement constraints are still valid at the bottom surface of the reconstructed geometries. Furthermore, gold foil is ductile enough for LiMn$_2$O$_4$ particles to be immersed in the substrate. Cathode particles slide and deform the ductile gold foil. Thus, the effect of pressing during sample preparation is negligible.

During galvanostatic discharge, it is assumed that the boundary flux is uniform over all of the active area. If we model electrolyte outside particles, we could have nonuniform boundary flux depending on particle geometries and Li-ion concentration in electrolyte. Before we investigate the intercalation-induced stress in real electrode microstructures, we apply the stress analysis to realistic particles without modeling electrolyte. Thus, we assumed that the boundary flux is uniform at particle surfaces. With this condition, the changes in the concentration of Li ions on the surface of
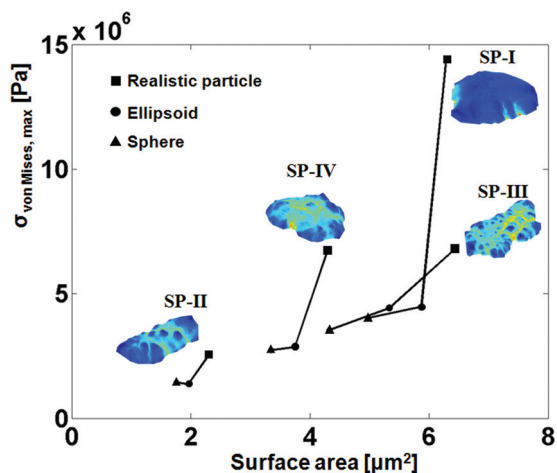
particles are the same for every portion of the surface in the particles due to uniform boundary flux, but the diffusion depth varies depending on particle geometries, which leads to nonuniform concentration gradient and consequently higher stress in realistic particles.

Compared to the bulk composite electrode, particle-based AFM scanning does not include the effect of inert materials (e.g., binder and conductive additives). For the bulk composite electrode, the binder materials can act as a structural buffer between active material particles when the active materials experience expansion or shrinkage during Li-ion intercalation/deintercalation. Also, the binder and conductive additives can block the reaction at the surface and thus reduce surface fluxes at bulk composite electrodes. In this paper, we focus only on the intercalation-induced stress in active materials. However, the finite element analysis presented in this paper could be easily extended by including inert material phases. Thus, the stress generation within the particle aggregates of active materials and inert materials could be further investigated.

The diffusion coefficient of Li ions is assumed to be constant. However, our prior work has shown that the diffusion coefficient of

Figure 11. (Color online) Maximum von Mises stress vs surface area in single particles, oblate ellipsoids, and spheres during 5 C galvanostatic discharge.
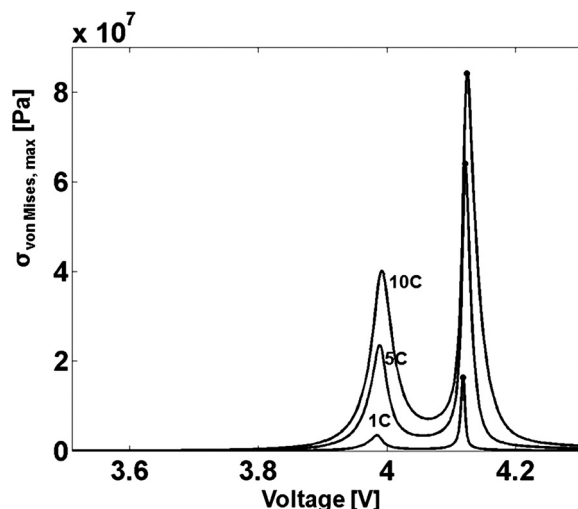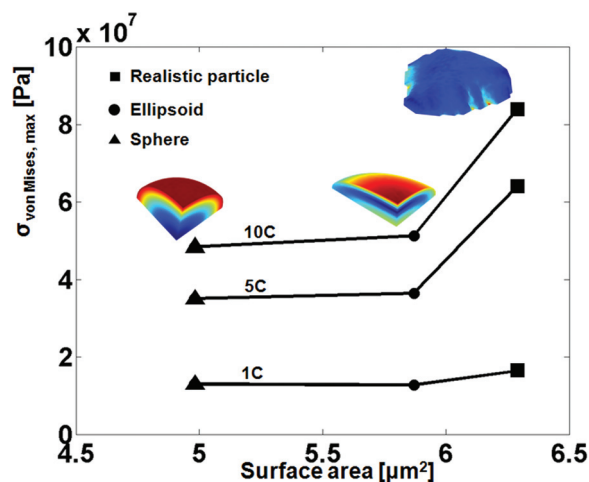

Figure 13. (Color online) Maximum von Mises stress in particle SP-I, oblate ellipsoid, and sphere by varying potentiodynamic charge rate.
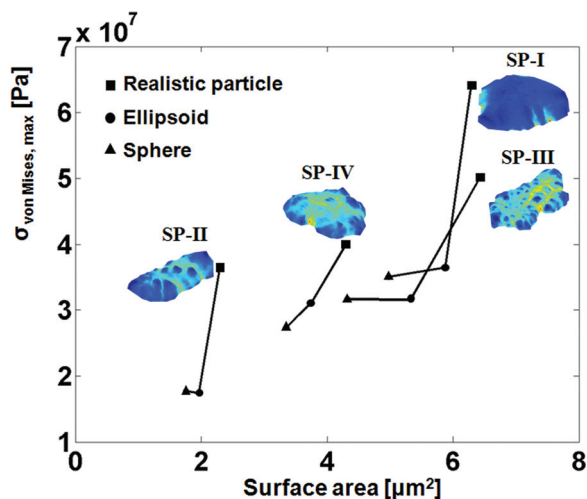
Figure 14. (Color online) Maximum von Mises stress vs surface area in single particles, oblate ellipsoids, and spheres during 5 C potentiodynamic charge.

$LiMn_2O_4$ particles varies depending on the state of charge.[22] It is also shown that the higher diffusivity enhances Li-ion diffusion resulting in lower stress, while lower diffusivity causes higher stress.[28] The W-shape Li-ion diffusivity[22] will slow down the Li-ion transport within the particles during cycling. Consequently, the state of charge (SOC)-dependent diffusivity can lead to the increase in diffusion-induced stress.

To investigate the local boundary flux in a real discharging condition, we used the pseudo-2D model based on solid-phase diffusion in spherical particles. Thus, the local Li-ion flux determined by the pseudo-2D model with spherical particles should differ from the boundary flux at the surfaces of realistic particles within the porous electrode. As revealed in the reconstructed particle geometry, the realistic particle has a larger surface area than the smooth particle. For the given concentrations of electrolyte and active materials, the reaction current density by Butler–Volmer equation decreases as the surface area increases. Thus, the actual local Li-ion flux would be lower than the value used here. In order to investigate the local distribution of stress and Li ions at microscale coupled with macroscale simulation, a multiscale modeling approach[29] should be adapted with the reconstruction of realistic microstructure in composite electrodes.

Intercalation-induced stress within realistic particles shows the stress concentration at V-shaped surfaces. For SP-I particle, the voxel mesh model has 40% larger surface area for boundary flux than the tetrahedral mesh and therefore the boundary flux of Li ion in voxel mesh is lower than that in tetrahedral mesh. Thus, the differences in surface area and boundary flux are likely to be the cause of the differences in discharge profiles between voxel and tetrahedral mesh, as shown in Fig. 7. The stiffness of the voxel element is lower than that of the tetrahedral element because the voxel (i.e., hexahedral) element has more degrees of freedom in shear loading. Thus, the stress in voxel mesh is higher than the stress in tetrahedral mesh. Jagged approximation of realistic geometry by voxel elements leads to a rugged variation in stress distribution even on smooth surfaces, while tetrahedral mesh shows smooth variation in von Mises stress distribution except at stress-concentrated boundaries. Tetrahedral mesh can reconstruct the realistic geometry using fewer nodes than voxel mesh requires. The voxel approach takes a larger number of Gaussian points for numerical integration and larger degrees of freedom than the tetrahedral approach and is computationally expensive. When three-dimensional analysis domains are discretized with tetrahedral elements the computational costs are low, compared to the costs
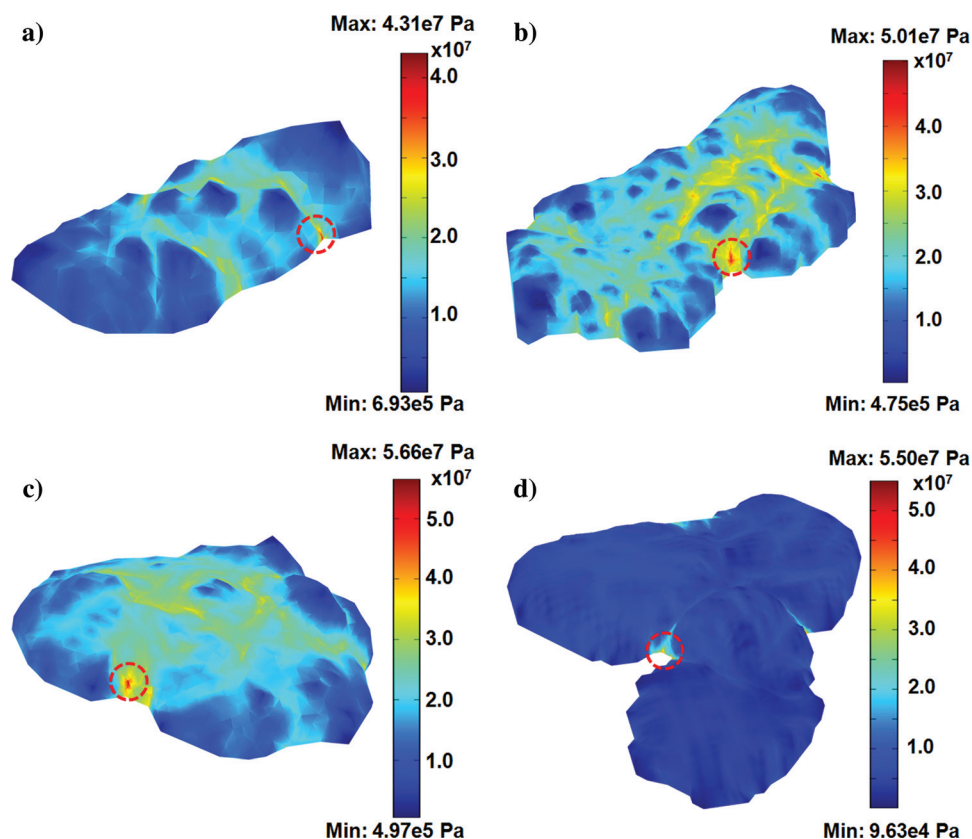

Figure 15. (Color online) von Mises stress distribution at the second peak under 5 C potentiodynamic half-cycle of charging: (a) SP-II, (b) SP-III, (c) SP-IV, and (d) MP-I.
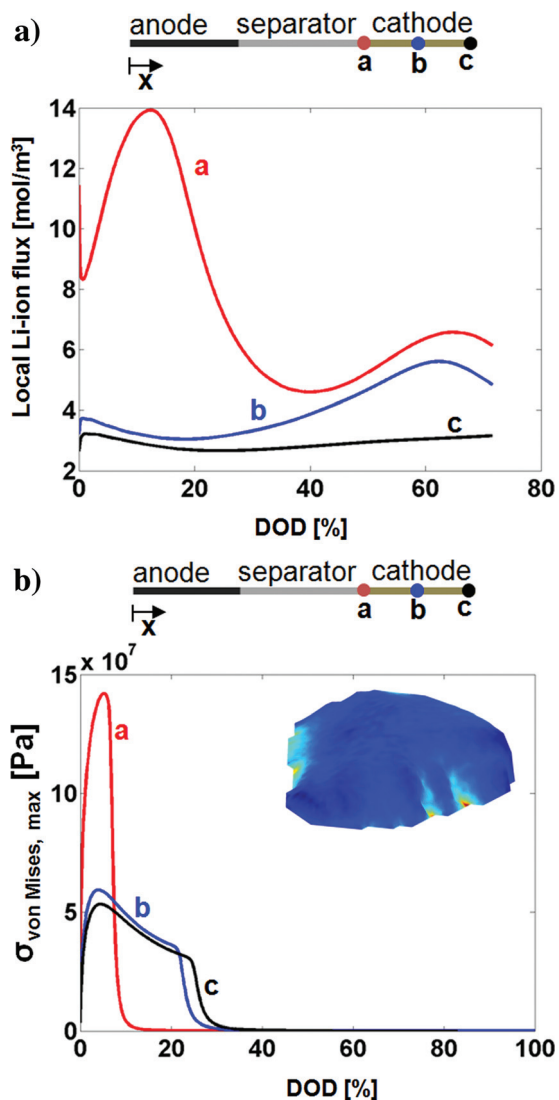
Figure 16. (Color online) (a) Local Li-ion flux at three different locations in the cathode under 5 C-rate discharge and (b) von Mises stress at point *B* in particle SP-I during the 5 C-rate discharge at macroscale.

of a hexahedral approach, making the tetrahedral approach more practical.

Even though the voxel mesh can artificially remove mesh singularity due to its uniformity, it results in artificially larger surface area. Thus, the tetrahedral mesh is preferable for intercalation-induced stress analysis in realistic particle structures that cause locally concentrated stress at complicated boundaries.

Conclusion

In this work, we scanned the surfaces of isolated electrode particles using AFM. The images attained from AFM scanning were then used to reconstruct the real particle structure geometries. Real-

istic particles have larger and more irregular surfaces than smooth ellipsoids and spheres. Simulation results show that the maximum von Mises stress in realistic particles is an order-of-magnitude higher than the stress in smooth particles and the particles near the separator experience higher stress and wider stress variations than those near the current collector in real discharging conditions. Due to surface ruggedness, stress concentration at the sharply dented region in realistic particles can increase the risk of the active material dissolving or fracturing, particularly near the separator. Voxel finite elements generate rugged surfaces even in smooth surfaces, which results in a larger surface area than in real geometry. Additionally, voxel finite elements require higher computational cost than tetrahedral elements. These results suggest that it is desirable to use tetrahedral mesh to achieve accurate surface reconstruction and intercalation-stress analysis of realistic particles at low computational cost.

References

1. P. Arora, R. E. White, and M. Doyle, *J.Electrochem. Soc.*, **145**, 3647 (1998).
2. Y. B. Yi, C. W. Wang, and A. M. Sastry, *J. Eng. Mater. Technol.*, **128**, 73 (2006).
3. J. Christensen and J. Newman, *J. Electrochem. Soc.*, **153**, A1019 (2006).
4. J. Christensen and J. Newman, *J. Solid State Electrochem.*, **10**, 293 (2006).
5. X. C. Zhang, W. Shyy, and A. M. Sastry, *J. Electrochem. Soc.*, **154**, A910 (2007).
6. X. C. Zhang, A. M. Sastry, and W. Shyy, *J. Electrochem. Soc.*, **155**, A542 (2008).
7. Y. T. Cheng and M. W. Verbrugge, *J. Power Sources*, **190**, 453 (2009).
8. H. F. Wang, Y. I. Jang, B. Y. Huang, D. R. Sadoway, and Y. T. Chiang, *J. Electroch. Soc.*, **146**, 473 (1999).
9. J. Zhou and P. H. L. Notten, *J. Power Sources*, **177**, 553 (2008).
10. D. Y. Wang, X. D. Wu, Z. X. Wang, and L. Q. Chen, *J. Power Sources*, **140**, 125 (2005).
11. H. Gabrisch, R. Yazami, and B. Fultz, *Electrochem. Solid-State Lett.*, **5**, A111 (2002).
12. M. R. Lim, W. I. Cho, and K. B. Kim, *J. Power Sources*, **92**, 168 (2001).
13. H. Gabrisch, J. Wilcox, and M. M. Doeff, *Electrochem. Solid-State Lett.*, **11**, A25 (2008).
14. J. Christensen, *J. Electrochem. Soc.*, **157**, A366 (2010).
15. S. Renganathan, G. Sikha, S. Santhanagopalan, and R. E. White, *J. Electrochem. Soc.*, **157**, A155 (2010).
16. S. Golmon, K. Maute, and M. L. Dunn, *Comput. Struct.*, **87**, 1567 (2009).
17. Y. Itou and Y. Ukyo, *J. Power Sources*, **146**, 39 (2005).
18. A. M. Stux, E. Gorzkowski, D. Rowenhorst, D. Stephenson, and D. R. Wheeler, *ECS Trans.*, **16**, 121 (2009).
19. S. Barnett, presented at the International Battery Association & Pacific Power Source Symposium, Hawaii, Jan.11–16, (2010).
20. P. R. Shearing, L. E. Howard, P. S. Jøgensen, N. P. Brandon, and S. J. Harris, *Electrochem. Commun.*, **12**, 374 (2010).
21. A. Clemencon, A. T. Appapillai, S. Kumar, and Y. Shao-Horn, *Electrochim. Acta*, **52**, 4572 (2007).
22. M. Chung, J. H. Seo, X. Zhang, and A. M. Sastry, *J. Electrochem. Soc.*, Submitted.
23. K. Terada, T. Miura, and N. Kikuchi, *Comput. Mech.*, **20**, 331 (1997).
24. S. J. Hollister and N. Kikuchi, *Biotechnol Bioeng.*, **43**, 586 (1994).
25. Y. H. Chen, C. W. Wang, G. Liu, X. Y. Song, V. S. Battaglia, and A. M. Sastry, *J. Electroch. Soc.*, **154**, A978 (2007).
26. M. Doyle, J. Newman, A. S. Gozdz, C. N. Schmutz, and J.-M. Tarascon, *J. Electrochem. Soc.*, **143**, 1890 (1996).
27. COMSOL Multiphysics Reference Guide, Version 3.5a (2008).
28. J. Park, W. Lu, and A. M. Sastry, *J. Electrochem. Soc.*, **158**, A201 (2011).
29. X. Zhang, Ph.D. Thesis, University of Michigan (2009).